



## ORIGINAL ARTICLE

# Rapid synthesis of bovine serum albumin-conjugated gold nanoparticles using pulsed laser ablation and their anticancer activity on hela cells



S.A Abdulateef<sup>a,f</sup>, Muna E. Raypah<sup>a</sup>, A.F. Omar<sup>a,\*</sup>, M.Z. Mat Jafri<sup>a</sup>,  
Naser M. Ahmed<sup>a</sup>, Noor Haida Mohd Kaus<sup>b</sup>, Azman Seeni<sup>c</sup>, Mohd Hafiz Mail<sup>d</sup>,  
Yasser Tabana<sup>e</sup>, Marawan Ahmed<sup>e</sup>, Sara Al Rawashdah<sup>e</sup>, Khaled Barakat<sup>e,\*</sup>

<sup>a</sup> School of Physics, Universiti Sains Malaysia, Gelugor, Penang, Malaysia

<sup>b</sup> School of Chemical Sciences, Universiti Sains Malaysia, Gelugor, Penang, Malaysia

<sup>c</sup> Advanced Medical and Dental Institute, Universiti Sains Malaysia, Kepala Batas, Penang, Malaysia

<sup>d</sup> Malaysian Institute of Pharmaceuticals and Nutraceuticals, National Institute of Biotechnology Malaysia, Gelugor, Penang, Malaysia

<sup>e</sup> Faculty of Pharmacy and Pharmaceutical Sciences, University of Alberta, Edmonton, AB, Canada

<sup>f</sup> College of Medicine, Al Iraqia University, 1556, Baghdad, Iraq

Received 17 April 2022; accepted 4 November 2022

Available online 10 November 2022

## KEYWORDS

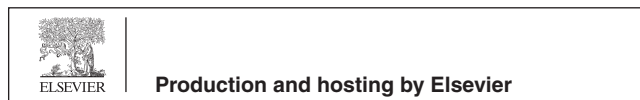
Gold Nanoparticles;  
Pulsed Laser Ablation;  
Bovine Serum Albumin;  
Localized Surface Plasmon  
Resonance;  
Cytotoxicity;  
Apoptosis

**Abstract** Nanoscience research aims to produce nanoparticles without adverse effects for medical applications. The pulsed laser ablation (PLA) technique was utilized in this study to synthesize gold nanoparticles (AuNPs) using bovine serum albumin (BSA) in simulated body fluid (SBF) at the fundamental wavelength of the Nd: YAG laser (1064 nm). BSA acted as a stabilizer, reducing and capping agent to produce spherically shaped AuNPs (diameter 3–10 nm). The successful synthesis of AuNPs was confirmed through color changes and UV–vis spectroscopy. The agglomeration and precipitation of AuNPs are attributed to the presence of BSA in the solution, and electrostatic repulsion interactions between BSA and Au nanoclusters. The effect of salt concentration of SBF on BSA stability as well as the interaction of BSA conjugated AuNPs to form complexes was studied using molecular dynamic simulations. Our results show that the stability of AuNPs-BSA conjugates increase with the salt concentration of BSA. Moreover, the synthesized AuNPs exhibit low toxicity and high biocompatibility, supporting their application in drug delivery. Investigation of the cytotoxic effect of the synthesized AuNPs show that normal fibroblast cells (L929)

\* Corresponding authors.

E-mail addresses: fairuz\_omar@usm.my (A.F. Omar), kbarakat@ualberta.ca (K. Barakat).

Peer review under responsibility of King Saud University.



remain intact after treatment whereas a dose-dependent inhibition effect on the growth of cervix cancer cells (HeLa) is observed. In general, this study presents an effective, environmentally-friendly, and facile approach to the synthesis of multifunctional AuNPs using the PLA technique, as a promising efficacious therapeutic treatment of cervical cancer.

© 2022 The Authors. Published by Elsevier B.V. on behalf of King Saud University. This is an open access article under the CC BY-NC-ND license (<http://creativecommons.org/licenses/by-nc-nd/4.0/>).

## 1. Introduction

Nanoparticles (NPs) have a variety of potential applications, particularly in the fields of biological sciences and biomedicine as a foremost vehicle for drug targeting and delivery (Amendola and Meneghetti 2013, Rehbock et al., 2014, Guerrini et al., 2018). Nanomedicine is a rapidly expanding field, and it is projected to be a promising tool for several therapeutic treatment programs. NPs can be utilized in nanocarrier-mediated combination treatments to modify multiple pathways, enhance the efficiency of therapeutic interventions, target specific phases of the cell cycle or overcome drug resistance mechanisms (Mitchell et al., 2021). Metal NPs are commonly synthesized, stabilized and functionalized by different chemical, physical, and biological techniques that comprise electrochemical reduction (Zhang et al., 2002), photochemical reactions (Scaiano et al., 2012), thermal decomposition (Lassenberger et al., 2017), and heat evaporation (Richter et al., 2011). The NPs synthesized via these techniques are particularly reactive, unstable, and hazardous to the environment (Singh et al., 2018), which has intensified the demand for green alternatives to the synthesis of NPs. In contrast, the green approaches are economical, eco-friendly, less time consuming, and are safe or non-invasive to the human body. These appealing properties have promoted the prevalence of green techniques in the synthesis of NPs (Freitas de Freitas et al., 2018). For instance, the microwave-induced plasma-in-liquid process (MWPLP) of synthesizing NPs does not require toxic reducing agents and the energy consumption is relatively low. Similar to radiolysis induced by gamma radiation or X-rays, the MWPLP basically involves the hydrolysis of water molecules by microwaves, which results in the production of reducing agents that initiate the nucleation of metallic particles (Čempel et al., 2018). Furthermore, the use of laser sources is another green route for the synthesis of NPs (Kabashin et al., 2010). For instance, Yb: KGW laser was used to synthesize biocompatible gold nanoparticles (AuNPs) with comparatively better morphology than their counterparts produced using other techniques (Correard et al., 2014).

The benefits of NPs includes low doses requirement to induce activity and their high bioavailability (Van der Zande et al., 2000, Jeevanandam et al., 2018). In order to generate a stable AuNPs in biological fluids, the NPs need to be coated, stabilized, functionalized, or conjugated with different organic moieties in order to create a protective layer surrounding the NPs that can subsequently prevent aggregation (Bogdanov Jr et al., 2015, Adewale et al., 2019). Practical applications of NPs in biological fluids, such as blood plasma, require the stability and monodispersity of the material under adverse conditions, since sedimentation and agglomeration of particles (Pérez-Juste et al., 2005, Dominguez-Medina et al., 2013) may disrupt biodistribution, resulting in damaging negative effects. Given that the concentration of ions in a simulated body fluid (SBF) is similar to that of the human blood plasma, SBF is utilized for in vitro analyses of the bioactivity of artificial materials and for the deposition of bone-like apatite on different substrates (Oyane et al., 2003).

Gold nanoparticles (AuNPs), in particular, has attracted interest among researchers especially in water purification for their catalytic properties (Harisha et al., 2021, Kim et al., 2021), colorimetric detection of targeted metal ion (Harisha et al., 2021, Nguyen et al., 2022) and due to its non-toxic and antibacterial properties, AuNPs has been employed in food nanopackaging (Paidari and Ibrahim 2021). Over the recent years, AuNPs has been employed in vast application in biome-

dicine. This include AuNPs potential application such as in radiosensitizing agent for cancer radiotherapy (Alhussan et al., 2021), as contrast agents in optical imaging, photoacoustic imaging, fluorescence imaging, computerized tomography and magnetic resonance imaging (Dheyab et al., 2022) and in cancer treatment mainly research on its anticancer activities conducted on cultured cell lines (Zhang et al., 2019, Li et al., 2021).

Cervical cancer disease is categorized as the fourth most commonly diagnosed cancer and the fourth major source of mortality in women due to cancer (Bray et al., 2018). In 2018, approximately 570000 cases and 311000 deaths from cervical cancer disease were estimated (Arbyn et al., 2020). Various treatment strategies such as chemotherapy, radiotherapy, and surgery have been employed for the treatment of cervix cancer. Chemotherapeutic therapy for cervical cancer reveals drug resistance-mediated side effects and poor diagnoses (Ordikhani et al., 2016) because the drugs are not targeted mainly at the cancer cells (Bromma and Chithrani 2020). NPs can surmount these constraints and substitute the advanced anticancer drugs. Currently, an active area of research is focused on the application of nanotechnology as a targeted delivery to cancer cells as a way to overcome drug resistance and to improve the efficacy of chemotherapeutic drugs (Xu et al., 2015). Furthermore, NPs with anticancer activity are safer compared to the currently available chemotherapeutic modalities.

In this context, gold nanoparticles (AuNPs) display exceptional conductivity, size-dependent properties, optical properties, less-toxicity, simplicity and high variations of functionalization (Ali et al., 2019). In the localized surface plasmon resonance (LSPR) wavelength region, AuNPs exhibit higher light absorption and scattering properties that strongly dependent on the size of the individual AuNPs and on their aggregation condition (Jain et al., 2006, Amendola et al., 2017). Color changes of AuNPs are extensively utilized as a sensing platform for chemical and biological targets (Upadhyayula 2012, Chansuvarn et al., 2015, Verma et al., 2015). An increase in the size or aggregation of AuNPs leads to a color change from burgundy to blue/purple. AuNPs conjugated with proteins via either covalent bonds or physical interactions offer a broad array of biomedical applications that include diagnosis, bio-imaging, conventional treatment interventions (Liu et al., 2019), and targeted drug delivery (Huo et al., 2012, Wahab et al., 2013).

Cancer nanotechnology is a versatile subject with extensive potential applications in cancer treatment, comprising molecular imaging and diagnosis, targeted treatment, and bioinformatics (Cai et al., 2008). AuNPs functionalized anticancer drugs such as doxorubicin (Baneshi et al., 2019) and cetuximab (Leve et al., 2019) have displayed advanced cellular uptake, efficacy, and destruction of breast and colon cancer cells. In recent times, AuNPs have garnered immense attention because of their considerable anticancer activities (Balasubramani et al., 2015, Daduang et al., 2015, Rajeshkumar 2016, Bhamidipati and Fabris 2017, Farooq et al., 2018, Patil et al., 2018, Patil et al., 2019, Qian et al., 2019, Sunderam et al., 2019, Wang et al., 2019, Zhang et al., 2019, Kalaivani et al., 2020, Vairavel et al., 2020, Al-Radadi 2021, Botteon et al., 2021, Shunmugam et al., 2021). AuNPs have shown anticancer effect against renal cell carcinoma (A498) (Liu et al., 2019), lung (A549) (Zhang et al., 2019), breast (MCF-7) (Sunderam et al., 2019), and cervix (HeLa) (Farooq et al., 2018, Patil et al., 2019, Qian et al., 2019) cancer cell lines. In addition, AuNPs are used to improve the uptake and effect of anticancer agents.

This study utilized pulsed laser ablation to synthesize AuNPs in an ionic solution resembling blood plasma. This green approach is a single step, rapid, cost-effective, and amenable to the functionalization of the synthesized AuNPs. In-situ and ex-situ self-assembly of AuNPs conjugated to bovine serum albumin (BSA) in simulated body fluid (SBF) that reduces aqueous Au ions was confirmed. Afterward, the bioactive elements of recombinant BSA in SBF for biosynthesis were identified, and the reaction mechanism underlying NPs biosynthesis was elucidated. The effect of salt concentration of SBF on BSA stability as well as the interaction of BSA conjugated AuNPs to form complexes was further studied using molecular dynamic simulations. Lastly, the cytotoxic effect of the synthesized AuNPs against human cervical cancer cells (HeLa) *in vitro* was also investigated.

## 2. Materials and methods

### 2.1. Preparation of simulated body fluid (SBF)

Using Kokubo's formulation, the SBF was prepared through the dissolution of reagent-grade mixtures of  $\text{CaCl}_2$ ,  $\text{K}_2\text{HPO}_4 \cdot 3\text{H}_2\text{O}$ ,  $\text{KCl}$ ,  $\text{NaCl}$ ,  $\text{MgCl}_2 \cdot \text{H}_2\text{O}$ ,  $\text{NaHCO}_3$ , and  $\text{Na}_2\text{SO}_4$  in distilled water and buffering at pH 7.25 with tris-hydroxymethyl aminomethane (THAM) and 1 N hydrochloric acid (HCl) at 37 °C.

### 2.2. Preparation of gold nanoparticles (AuNPs)

The pulsed laser ablation (PLA) technique was used to synthesize AuNPs in SBF on a gold plate (purity 99.99 %) as shown in Fig. 1. Nd:YAG pulsed laser was utilized as the light source with a fundamental wavelength of 1064 nm, 650 mJ per pulse, a spot size of 3 mm<sup>2</sup>, a repetition rate of 5 Hz, and six pulse duration. The laser was centered using a focusing lens with a focal length of 100 mm on an Au plate and was placed at the bottom of a 10 mL quartz vessel filled with 3 mL of SBF. PLA in SBF was conducted for 8 min at a repetition rate of 5 Hz. BSA (98 % lyophilized powder, MW = 66,430 Da)

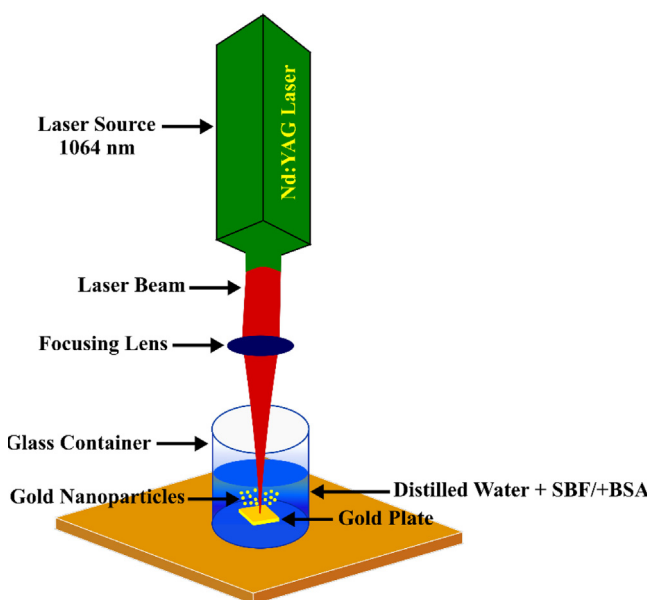


**Fig. 1** Schematic diagram of the preparation of AuNPs using pulsed laser ablation system.

was procured from Nacalai Tesque (Kyoto, Japan). The mass of the synthesized AuNPs were measured using Semi-micro analytical balance GR-200 (A&D Company Ltd, Japan). This was done to determine the final concentration of the synthesized AuNPs in the solution by measuring the difference in gold plate mass before and after the ablation has taken place.

### 2.3. Conjugation of bovine serum albumin (BSA)

A fresh solution of BSA stock was prepared for each experiment or stored at -2 °C otherwise to decrease the aggregation of protein and sedimentation. The BSA concentration was set at 375 μM for both ex-situ and in-situ bioconjugations. In the ex-situ experimental setup, the BSA was added to the SBF solution after the ablation process (after the AuNPs has been synthesized) to determine the effect of ex-situ BSA bioconjugate on the dispersion and size of synthesized NPs. On the other hand, for the in-situ experimental setup, the laser ablation on the gold plate was performed in the solution containing both SBF and BSA.

### 2.4. Spectral analysis

The spectral absorbance data (200–880 nm) of the AuNPs solutions were obtained under ambient conditions (25 °C) using a modular UV–vis Jaz Spectrometer (Ocean Optics, Largo, FL, USA).

### 2.5. Transmission electron microscopy (TEM)

Microscopic images of the samples were obtained using transmission electron microscopy (TEM, FEI CM 12, Hillsboro, OR, USA) operated at 120 kV and high-resolution TEM (HRTEM) at 200 kV with a field emission electron microscope (TECNAI G2 20 S-TWIN, FEI). To determine the concentration of AuNPs, it was essential to measure the weight of the gold target separately both before and following each radiation phase for each sample.

### 2.6. Anticancer activity

#### 2.6.1. Cell culture

L929 and HeLa cells were acquired from ATCC (Manassas, VA, USA). Minimum Essential Medium (MEM) and Dulbecco's Modified Eagle Medium (DMEM) supplemented with 10 % of heat-inactivated fetal bovine serum (FBS) together with 1 % sodium pyruvate and penicillin–streptomycin were utilized. MEM and DMEM were used to culture L929 cells and HeLa cells, respectively, at 37 °C in a humidified atmosphere incubator with 5 % CO<sub>2</sub>.

#### 2.6.2. Cell viability assay

MTT assays were utilized to determine cell viability using the HeLa cell line. The freshly prepared MTT reagent using 5 mg of sterile phosphate-buffered saline (PBS) was filtered through a 0.2-μm syringe filter and afterward subjected to dilution in a fresh culture medium to achieve a final concentration of 500 μg/mL. The aged culture medium was aspirated cautiously through a vacuum pump. 200 μL of culture medium containing MTT reagent was then added to the sample before being

subjected to incubation for 3–5 h. After the incubation, the supernatant was aspirated, and the water-insoluble Formosan salt was solubilized in 200  $\mu\text{L}$  of dimethyl sulfoxide (DMSO) in each well. Following 10 min of incubation at 37  $^{\circ}\text{C}$ , a microplate reader (Thermolab Systems 354, Helsinki, Finland) was used to measure the optical density (OD) at a primary wavelength of 570 nm and a reference wavelength of 650 nm. The cell viability at each concentration was calculated as a percentage using the underlying equation (Eq. (1)):

$$\text{Cellviability}(\%) = \left( \frac{\text{Sampleabs}_{570\text{nm}} - \text{Sampleabs}_{650\text{nm}}}{\text{Controlabs}_{570\text{nm}} - \text{Controlabs}_{650\text{nm}}} \right) \times 100\% \quad (1)$$

A control was prepared devoid of AuNPs treatment, and 50 % of cell inhibition at a specific concentration of AuNPs was expressed as  $\text{IC}_{50}$ . Different concentrations of the samples being tested were utilized for the estimation of  $\text{IC}_{50}$  values. After plotting a curve of cell viability against the sample concentrations based on prior studies (Tabana et al., 2016),  $\text{IC}_{50}$  was calculated.

### 2.7. Apoptosis assay

Apoptosis initiated by PSLE was studied using the Annexin V labeling BD Annexin-V-FITC Assay Kit (BD, Franklin Lakes, NJ, USA). The BDFac Canto II Flow Cytometer and BD Fac-Diva were utilized for data acquisition and analyses, respectively. The treated cells were washed two times with PBS. A total of 5,105 cells were amassed via centrifugation at 1500 rpm and 24  $^{\circ}\text{C}$  for a duration of 5 min. Cells were then stained with 5  $\mu\text{L}$  of annex in-V conjugated with fluorescein isothiocyanate (FITC) and 5  $\mu\text{L}$  of propidium iodide (PI) in the dark under ambient conditions for 15 min. Cells were analyzed by flow cytometry-based on FITC and PI fluorescence intensity. Untreated cells served as the negative control. A minimum of 10,000 events were collected for each sample.

### 2.8. Molecular modelling workflow

#### 2.8.1. Structural preparation of Au(111)BSA complexes

The crystal structure of bovine serum albumin (BSA) (PDB code: 4F5S) was downloaded from the RCSB PDB (Berman et al., 2000). The protein was then prepared for MD simulations using the Molecular Operating Environment (MOE 2019) software (Bujacz 2012). At the beginning of this preparation step, all missing heavy atoms in the initial BSA structure were included, all hydrogen atoms were added according to the proper protonation states of all ionizable residues and valences at the physiological pH (pH = 7). Finally, the heavy atom displacement was minimized to a maximum of 0.5 Angstrom. The prepared PDB file was then saved from MOE for the subsequent phases of the computational workflow, which involved MD simulations.

With respect to the preparation of the Au-BSA complexes, the PropPDB utility program as implemented in the CPPTRAJ utility of AMBERTools (Roe and Cheatham III 2013) was used to build a 140x120x10 rectangular slab of Au (111). Ten varying orientations of the BSA protein structure were placed over the Au(111) slab using UCSF Chimera software [ref]. Accordingly, each Au-BSA complex was inserted in a box of explicit TIP3P water molecules and was neutralized

with counterions. To also study the effect of increasing salt concentrations on the stability of BSA adsorption to the Au (111) surface, 10 additional Au-BSA complexes were prepared with adequate  $\text{Na}^+$  ( $\sim 469$ ) and  $\text{Cl}^-$  ( $\sim 455$ ) ions to attain a concentration of 150 mM. The AMBER-ff19SB (Tian et al., 2019) forcefield and the interface V1.5 forcefield (Heinz et al., 2013) were utilized for the protein component and Au(111), respectively. For the two negative control simulations of each salt concentration, the same crystal configuration of BSA utilized in the Au-BSA complexes was simulated under similar settings but without the presence of the Au(111) slab in the simulation box.

#### 2.8.2. Molecular dynamics simulation protocol

For each system, the MD simulation protocol was implemented using the following steps; each system was initially minimized into four successive stages. The first stage involved the minimization of solvent atoms and ions for 5000 cycles of steepest descent (SD) accompanied by further 5000 cycles of conjugate gradient (CG) minimization with 100  $\text{kcal mol}^{-1}$  restraints on protein-heavy atoms and Au(111) atoms. Two more cycles of minimization were conducted on each system (5000 SD & 5000 CG minimizations) in the presence of 50  $\text{kcal mol}^{-1}$  and 5  $\text{kcal mol}^{-1}$  restraints on protein-heavy atoms and Au(111) atoms. A final minimization step was carried out for the same number of steps and minimization protocol with only 0.5  $\text{kcal mol}^{-1}$  restraints on Au(111) atoms. Following minimization, each system was heated for 100,000-time steps (1 fs) to reach 300 K in the canonical NVT ensemble (i.e. constant number of particles, volume, and temperature) with 5  $\text{kcal mol}^{-1}$  restraints on the protein-heavy atoms and on the Au(111) atoms. Each system was then subjected to an additional equilibration step in the NPT ensemble (constant number of particles, pressure, and temperature) for 10 ns and using an integration time step of 2 fs in the presence of 0.5  $\text{kcal mol}^{-1}$  restraints on Au(111) atoms only. Finally, a 100 ns ( $5 \times 20$  ns trajectories) production MD simulation stage was carried out for each system while implementing a 0.5  $\text{kcal mol}^{-1}$  restraint on the Au(111) atoms. The particle mesh Ewald (PME) (Darden et al., 1993) technique was used to compute the long-range electrostatic interactions, while the SHAKE algorithm was utilized to confine the mobility of hydrogen-containing bonds. The entire simulations were conducted under periodic boundary conditions. The simulations were performed using pmemd. CUDA, a GPU-enabled executable (Pierce et al., 2012) in the AMBER20 suite (Salomon-Ferrer et al., 2013).

#### 2.8.3. Clustering and analysis of MD simulations

Clustering based on backbone RMSD was performed by DBSCAN (Shao et al., 2007) using the cpptraj module of AMBERTools (Roe and Cheatham III 2013). For the entire 20 simulations of the Au-BSA complexes, frames of the last 50 ns of the 100 ns simulations were used after stripping ions and water molecules from the trajectory. The distance cutoff between points to distribute clusters,  $\epsilon$ , was set to 3.0 and the centroid of the top-ranked clusters was used in a succeeding interaction analysis. All secondary structure analysis, root-mean-square deviations (RMSD), and atomic positional fluctuations (RMSF) of the bound proteins were conducted by means of the CPPTRAJ module (Roe and Cheatham III

2013) of AMBERTools. Salt bridges analysis was finally carried out using the salt bridge plugin of VMD software (Humphrey et al., 1996).

### 2.9. Statistical analysis

The entire experiments were conducted in triplicates. One-way analysis of variance (ANOVA) accompanied by Dunnett's tests was utilized to statistically analyze the results. Results are presented as mean values of three independent experiments ( $n = 3$ ) and standard deviation (SD). The threshold for significance was a  $p$ -value of  $< 0.05$ .

## 3. Results and discussion

In general, when PLA is carried out in the water, a colloidal solution of NPs that is unstable with a relatively broad size distribution is produced. The sizes of synthesized NPs are dependent on the laser parameters that include wavelength and pulse energy, type of liquid, and type of metal (Hedei et al., 2019, Tan et al., 2019). Solutes (additives) can either modify the physical and chemical properties of the liquid solution or interface with the ablated material, physically and chemically. The inclusion of solutes to the liquid, where PLA is carried out, directly affects the cavitation bubble (Amendola and Meneghetti 2013) and the confinement of the plasma plume (Furusawa et al., 2004) as the solute influences viscosity, tension, and density of the solvent. Adding BSA to the SBF increased the viscosity, thus extending the lifespan of the bubbles generated during PLA.

Partial oxidation results in the distribution of  $\text{Au}^+$ ,  $\text{Au}^{+3}$ , and metallic  $\text{Au}^0$ . It is important to note that laser-generated AuNPs act as electron acceptors. Zeta potential measurements indicated that the entire laser-generated AuNPs in pure water are negatively charged. Earlier studies showed that positively charged Au surfaces are drawn to diverse species that include  $\text{H}_2\text{O}$  molecules, oxygen, and  $\text{CO}_2$  to form a pH-dependent equilibrium of  $\text{Au-OH/Au-O}^-$  and  $\text{AuCO}^- - 3$  groups (Sylvestre et al., 2004, Rehbock et al., 2014). These surface charges generate a stable colloidal solution via an electrostatic stabilization effect. Stabilizing agents avert the agglomeration of particles through physically affixing to the NPs (i.e., capping), which have an effect on the charges and/or lead to steric stabilization.

### 3.1. Absorption spectra

UV-vis absorption spectroscopy is an extensively utilized technique to investigate the optical properties of AuNPs and to assess the interactions between NPs and proteins. These interactions alter the absorption spectra of AuNPs, and the resulting changes can be used to elucidate binding properties. Changes in the wavelength and bandwidth of the absorption spectra of the NP-protein complex are dependent on the size, clustering, and local dielectric environments of AuNPs. Precipitates of colloidal AuNPs from the SBF solution are formed at a physiological pH. The UV-vis spectra displayed in the Fig. 2 (a) is also known as extinction spectra, where they are the results from the combination between plasmon absorption plus nanoparticle scattering. The blue line in Fig. 2(a) represents the synthesis of colloidal AuNPs for the sample prepared

at an intensity of  $358.4 \text{ J/cm}^2$  in the SBF solution. There is a strong indication from the obtained spectra as a function of time that there is an aggregation of particles in the early phases of precipitation after preparation, denoted by the broadening of the plasmon band. The spectra were obtained after equilibration for a duration of 10 min. For a faster visualization, the time-dependent spectra were acquired for BSA at high concentration and ionic strength. From the TEM images shown in Fig. 2(e – h), the best separation of the AuNPs with narrow size nanoparticles occurs when the AuNPs were synthesized using laser ablation in the SBF + BSA solution (shown in Fig. 2 (e)) where the addition of the BSA successfully assist in preventing particles from aggregation. The protein corona was discovered to regulate nanoparticles interaction with the surroundings (Roy et al., 2019), and subsequently enhanced the stability of the colloidal AuNPs by preventing their aggregation in the saline solutions (Abdulateef et al., 2017). This phenomenon is displayed in Fig. 2(f). In ex-situ bio-conjugation, the BSA was added to the colloidal AuNPs (with SBF) after the ablation process took place. As a result, the formation of chain-like cluster of AuNPs can be observed as shown in Fig. 2(g). Hence, in the production of stable AuNPs, it is primarily important to immediately minimise the aggregation of the NPs after the ablation process in producing stable AuNPs. With the absence of the BSA, the aggregation of the AuNPs happen drastically and formed a larger cluster of particles as shown in Fig. 2(h).

The high ionic strength of BSA is shown to be a key factor that initiates precipitation and agglomeration during ablation time and on a shorter time after the process. The redshift of the plasmon peak can be attributed to plasmon coupling within aggregates of AuNPs. This red-shift band dissipates as the aggregates are precipitated out of the solution. An increase in agglomeration, sedimentation, and crystallization of larger particles is denoted by a transparent pale purple color.

Absorption spectra were obtained for the ex-situ AuNPs and BSA after laser ablation, the inclusion of BSA at the physiological concentration ( $375 \mu\text{M}$ ) and following the adsorption of AuNPs on BSA. Plasmon coupling with aggregates of AuNPs causes a decrease in the LSPR absorption spectrum, broadens the plasmon band, and initiates a redshift in the LSPR peak. SBF with a medically applicable pH and ionic strength was utilized to elucidate the fundamental mechanism of AuNPs precipitation during the laser ablation process. The PLA process with an ionic strength comparable to that of water leads to dissociation into cations and ions, with the ions binding to the AuNPs' surface. As a result, the neutralization of the surface charge and initiation of the instant and unalterable agglomeration of AuNPs into a large structure (observed as a precipitate). Hence, the aggregation and precipitation AuNPs is dependent on the ionic strength of SBF. Therefore, it is crucial to stabilize the early aggregates and constrain the clustering of AuNPs in order to control the aggregate size and prevent precipitation of AuNPs. The transparent lavender color of the sample (Fig. 2) denotes significant aggregation or larger AuNPs and high stability in the harsh SBF medium in the presence of BSA.

UV-vis spectra were acquired for the colloidal dispersion of in-situ AuNPs and BSA system. These spectra were measured 1 hr after the pulse laser ablation of BSA-conjugated AuNPs in SBF. Fig. 2 (red line) shows the significance of the absorption

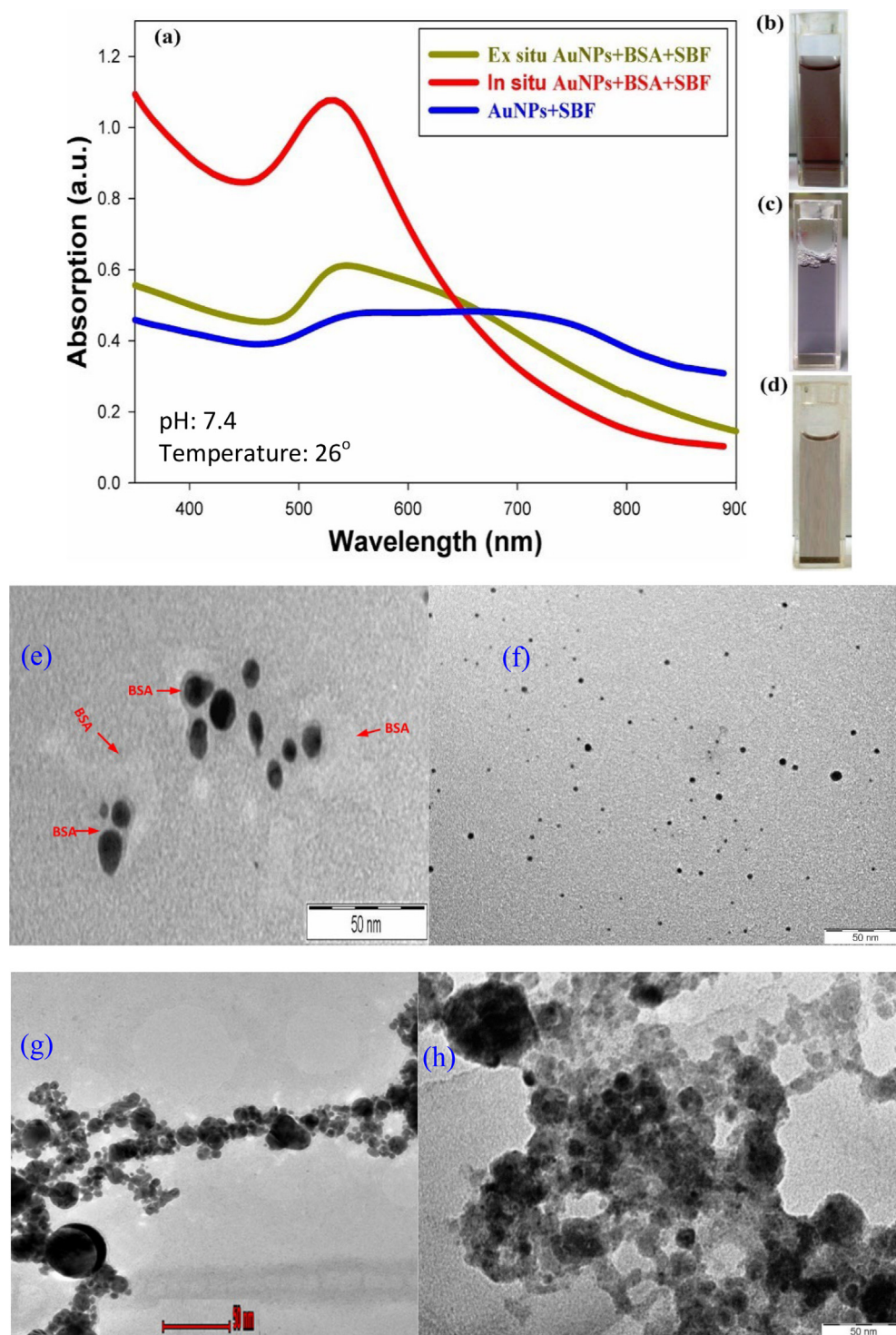


**Fig. 2** UV-vis spectra of the colloidal dispersion containing particles synthesized by means of laser ablation of an Au target in-situ (red line) and ex-situ (green line) at a laser fluence of  $358.4 \text{ J/cm}^2$ . Blue curve is the absorbance spectrum of AuNPs and SBF. Inset figure shows the images of: (b) in-situ AuNPs + SBF + BSA, (c) ex-situ AuNPs + SBF + BSA, and (d) AuNPs + SBF. Transmission electron microscope images of (e) in situ AuNPs + SBF + BSA, (f) BSA proteins adsorb to AuNPs synthesized by laser ablation in SBF In- situ (g) ex-situ AuNPs + SBF + BSA, and (h) AuNPs + SBF.

peak at 529 nm, which was related to the LSPR of the AuNPs. In this figure, the transparent deep pink color of the sample indicates a stable sample which can be attributed to the

insignificant aggregation and intensive stability in the harsh SBF medium in the presence of BSA. In both cases (i.e. ex-situ and in-situ) the conjugation of BSA to AuNPs is depen-

dent on the ionic strength of SBF, since the presence of salt increases binding affinity due to an overall increase in the hydrophobicity of AuNPs (Dominguez-Medina et al., 2013, Abdulateef et al., 2017).

### 3.2. Stability of AuNPs

The stability of AuNPs is a significant feature for biomedical applications. Following preparation of the suspension, UV-vis spectra were obtained for AuNPs conjugated to BSA in SBF at a laser fluence of  $358.4 \text{ J/cm}^2$  after 1, 2, 3, and 4 weeks of incubation at  $-2^\circ \text{C}$ , as plotted in Fig. 3. The LSPR band of AuNPs is dependent on the surrounding medium, interparticle distance, and morphology and size of NPs. An increase in the size, aggregation, or agglomeration of NPs is indicated by a red shift in absorbance, which is denoted by the blue color of the solution, a phenomenon referred to as Ostwald ripening effect. Interestingly, between all-time points, there is no considerable variation in the spectra, and the maximum absorption wavelength ( $\lambda_{max}$ ) remains constant (529 nm) (Irfan et al., 2020). This result confirmed the long-term stability of AuNPs in SBF. In order to have a better view on the potential spectral aging of the AuNPs, the relationship between absorbance at 529 nm across the 4 weeks of spectroscopic measurement of the sample was also plotted in the same figure. From the graph, it shows that the peak spectrum only fluctuates between 1.169 (week 0) and 1.108 (week 4) absorbance value, indicating a good stability of the synthesized AuNPs.

### 3.3. High-resolution transmission electron microscopy (HR-TEM)

To study the effect of the media surrounding during PLA on the properties of AuNPs, a series of colloids were prepared at the basic laser wavelength and laser fluence of  $3583.4 \text{ J/cm}^2$ . The crystal structure of in-situ AuNPs conjugated with BSA in SBF at a laser fluence of  $358.4 \text{ J/cm}^2$  obtained using HR-TEM images is presented in Fig. 4. The morphology of AuNPs is displayed in Fig. 4(a). The AuNPs are sphere-shaped or spherical-like and distinct. As shown,

in Fig. 4(b), the mean diameter of AuNPs was approximately 8 nm, with a narrow size range and a standard deviation

of 1.44. The HR-TEM images show the fringe spacing and crystallographic planes of single nanoparticles (measured d-spacing of 0.235 nm) of AuNPs, as depicted by Fig. 4(c).

The selected area electron diffraction (SAED) pattern of a distinctive AuNPs characterized with (111), (200), (220), and (311) peaks is displayed in Fig. 4(d). The SAED pattern reveals the presence of a cubic Au phase (PDF#04-0784) with a lattice parameter of 0.39 nm. SBF contains high concentrations of NaCl electrolyte that dissociates when added to water into  $\text{Na}^+$  and  $\text{Cl}^-$ , with  $\text{Cl}^-$  interacting with AuNPs. Since 3.3–6.6 % of the surface atoms that exist on laser-generated particles are oxidized to Au-O (Yamada et al., 2007), the increase in surface charge partly stems from the interfacing of the surface OH groups with Cl surface groups, which neutralizes the surface charge, and stimulates an immediate and permanent agglomeration of AuNPs into large structures of dark gray precipitates. However, it is crucial to stabilize early aggregates and constrain the agglomeration of AuNPs to control their aggregate size and avoid the formation of AuNPs precipitates. Hence, BSA was directly incorporated into AuNPs following the PLA process. BSA is capable of adsorbing onto AuNPs, as observed in a previous study (Tsai et al., 2011).

### 3.4. Dynamic light scattering (DLS)

The DLS results are represented in intensity-weighted size distribution. The important parameter obtained from DLS is the z-average particle size (Dz). In DLS, the scattered light intensity of a particle increases as the particle size increases. In the ex situ analysis, during pulse laser ablation in SBF, the high ionic strength resulted in the formation of a salt bridge between AuNPs to yield cluster of AuNPs. After ablation and the direct addition of BSA, AuNPs exhibited adsorption of BSA and effectively stopped agglomeration and sedimentation of the AuNPs. The DLS results for AuNPs conjugated to BSA in SBF. In the ex situ analysis, the z-average size Dz was 980 nm and the polydispersity (PDI) was 0.865. In the in-situ analysis, Dz was 145 nm and PDI was 0.321. The DLS results for ex situ and in situ analysis are shown in Fig. 5.

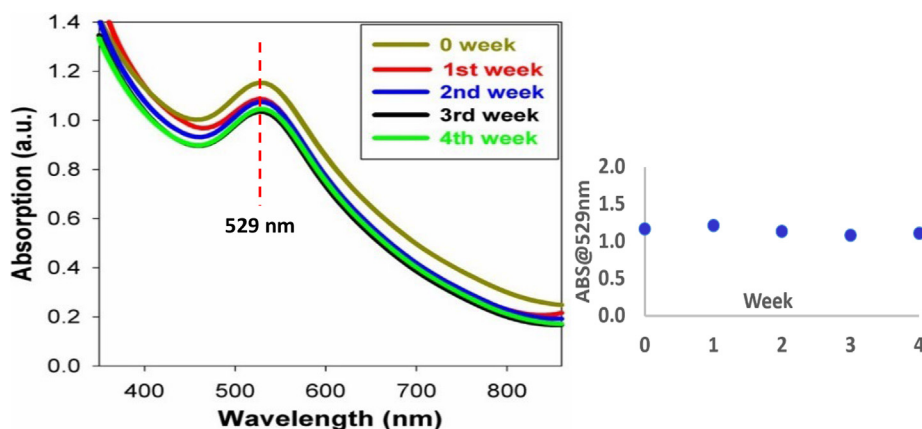
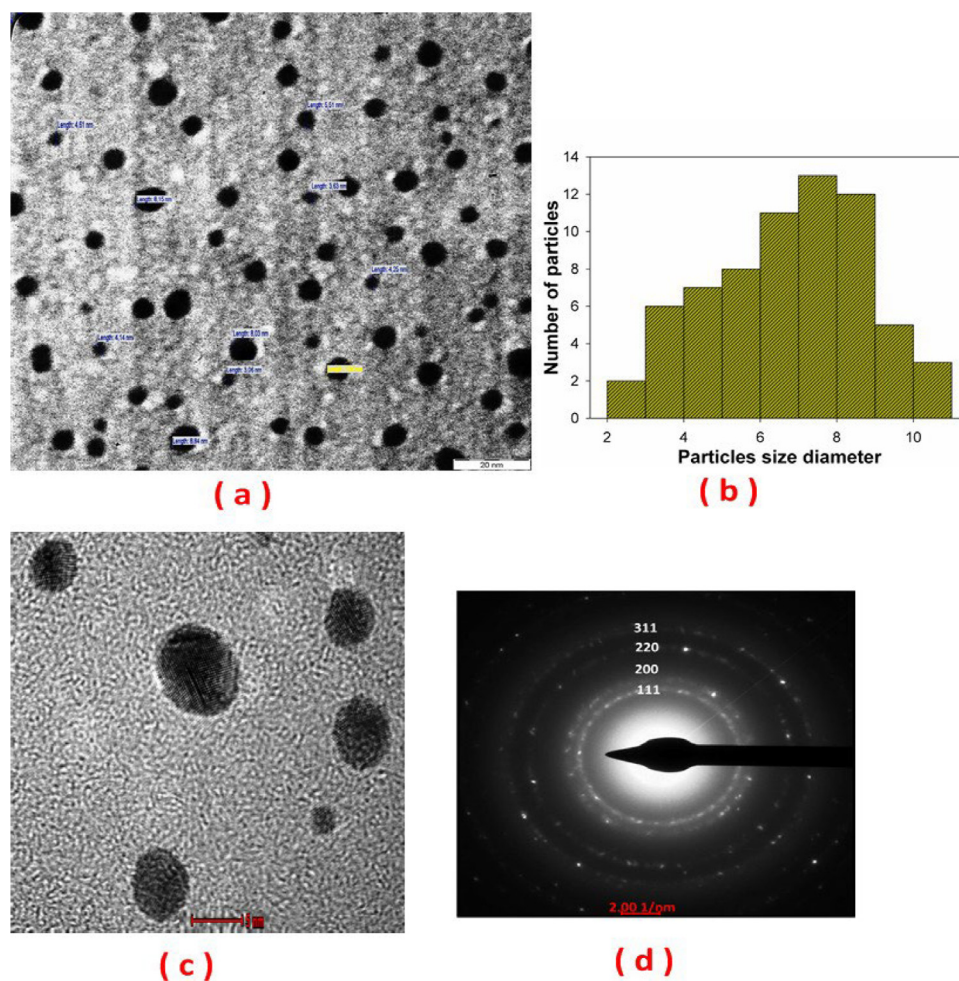
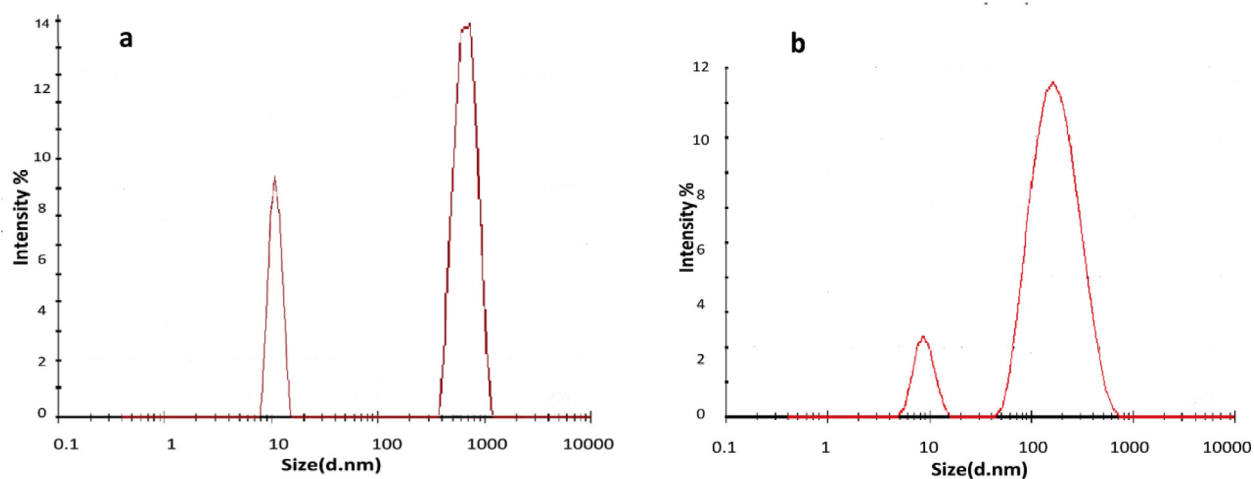


Fig. 3 UV-vis spectra measured after 1, 2, 3, and 4 weeks for the AuNPs conjugated to BSA in SBF at laser fluence of  $358.4 \text{ J/cm}^2$ .



**Fig. 4** TEM and HR-TEM of in-situ AuNPs conjugated with BSA in SBF at a laser fluence of  $358.4 \text{ J/cm}^2$ : (a) morphology, (b) particles size distribution, (c) fringe spacing of  $0.23 \text{ nm}$ , and (d) SAED pattern indicating face-centered cubic crystal structure corresponding to the gold.



**Fig. 5** Colloidal AuNPs distribution according to DLS for (a) ex-situ and (b) in-situ AuNPs conjugated to BSA in SBF.

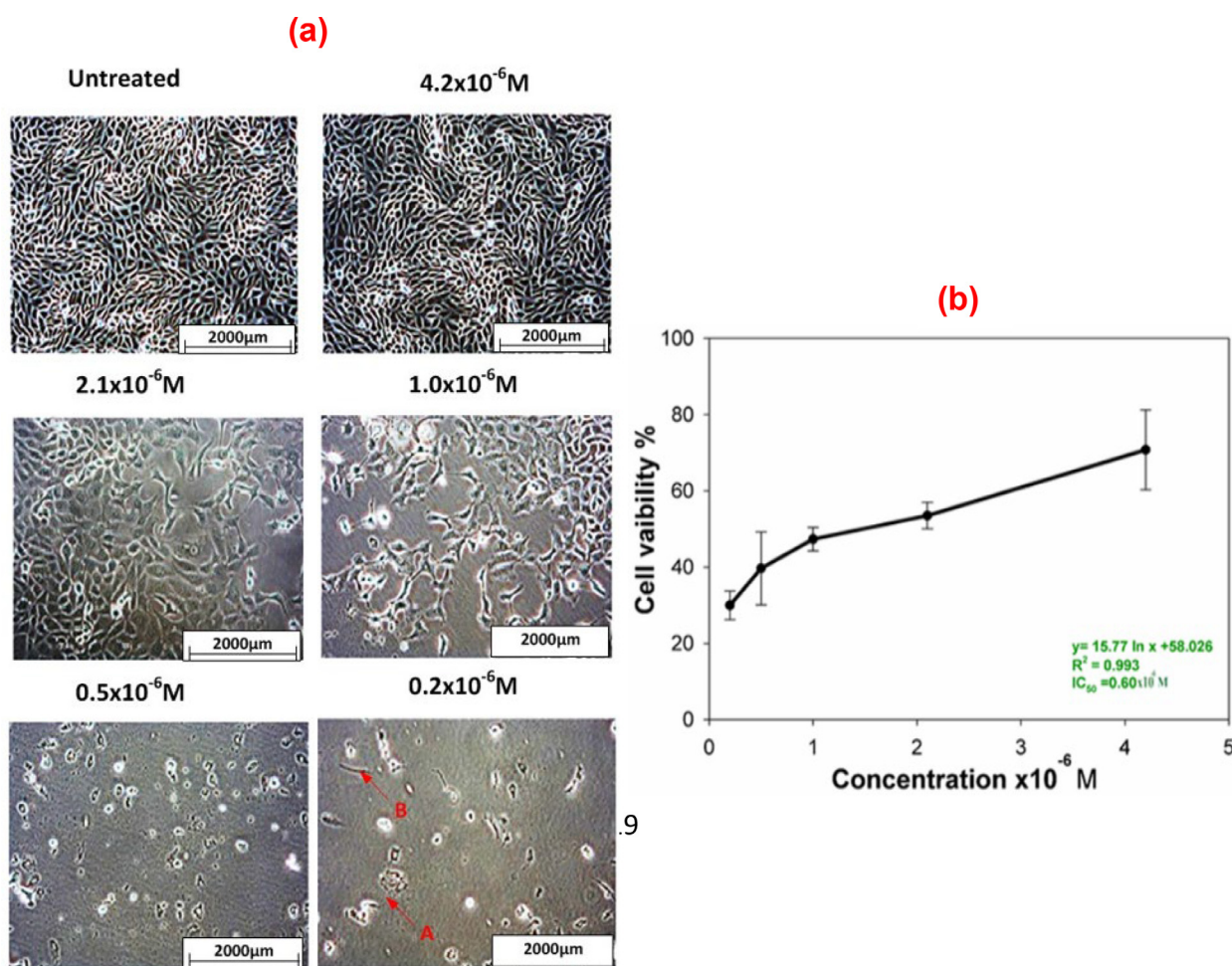


**Fig. 6** Dose-dependent cytotoxicity of the AuNPs conjugated BSA in SBF on HeLa cell line: (a) morphology of HeLa cells with and without AuNPs treatment at a magnification of 20x and (b)  $IC_{50}$  value of the AuNPs conjugated BSA in SBF on HeLa cell line.

### 3.5. Cytotoxicity of BSA-conjugated AuNPs in SBF

Cytotoxic effects of synthesized AuNPs conjugated to BSA in SBF were investigated for HeLa cancer cells based on cell viability using MTT assay. Dose-dependent cytotoxicity ( $0.2 \times 10^{-6}$ ,  $0.5 \times 10^{-6}$ ,  $1.0 \times 10^{-6}$ ,  $2.1 \times 10^{-6}$ , and  $4.2 \times 10^{-6}$  M) of AuNPs-treated HeLa cells are presented in Fig. 6. The medium comprising only SBF and BSA was used as negative control (untreated sample). Fig. 6(a) shows that the cytotoxic effect on HeLa cells increases with decreasing concentration of AuNPs. The cell viability of 84 % and 33 % was achieved at concentrations of  $4.2 \times 10^{-6}$  and  $0.2 \times 10^{-6}$ , respectively. As shown in Fig. 6(b), the  $IC_{50}$  was determined to be  $0.6 \times 10^{-6}$  M. The charged BSA may adsorb to the surface of AuNPs, and this adsorption or adhesion has been quantitatively analyzed for BSA in a prior report (Sagvolden 1999). The properties of BSA influence the uptake by tissues via molecule binding to surface-bound ligands (Torchilin 2011). The proteins are usually dormant and have a lengthy circulation duration in vivo. Nonetheless, a minor stimulus, such as a slight modification in pH, can cause a variation between the “sticky and stealthy” phenotype (Li et al., 2010, Pelaz et al., 2017). The results imply that AuNPs conjugated to

BSA in SBF might be valuable nano-carrier for the slow release of anticancer drugs. This study is at the forefront of evaluating the cytotoxic effect of AuNPs conjugated to recombinant BSA on cancer cells.

Although high concentrations of nanostructures have been utilized for toxicity studies, which are usually inappropriate for humans, AuNPs can be employed at a low concentration to control cell growth and proliferation with negligible adverse health effects (Hussain and Schlager 2009).

The cytotoxicity of AuNPs conjugated BSA in SBF was also examined on the L929 cell line (normal cells) with the aim of testing cell viability using the MTT assay. Dose-dependent cytotoxicity ( $0.2 \times 10^{-6}$ ,  $0.5 \times 10^{-6}$ ,  $1.0 \times 10^{-6}$ ,  $2.1 \times 10^{-6}$ , and  $4.2 \times 10^{-6}$  M) was also tested on AuNPs-treated L929 cells. The SBF + BSA medium was used as the negative control (untreated sample). Fig. 7(a) presents the cytotoxicity assay result for AuNPs conjugated with BSA in SBF at laser fluence 358.4 J/cm<sup>2</sup> on L929 cells. Evidently, the AuNPs did not exhibit a significant cytotoxic effect on L929 cells. The cell viability results at concentrations of  $0.2 \times 10^{-6}$  M and  $4.2 \times 10^{-6}$  M was 107 % and 116 %, respectively. It can be inferred that the treatment was not cytotoxic to normal cells at the concentrations used. Fig. 7 shows that the treatment with synthesized AuNPs does not induce a con-

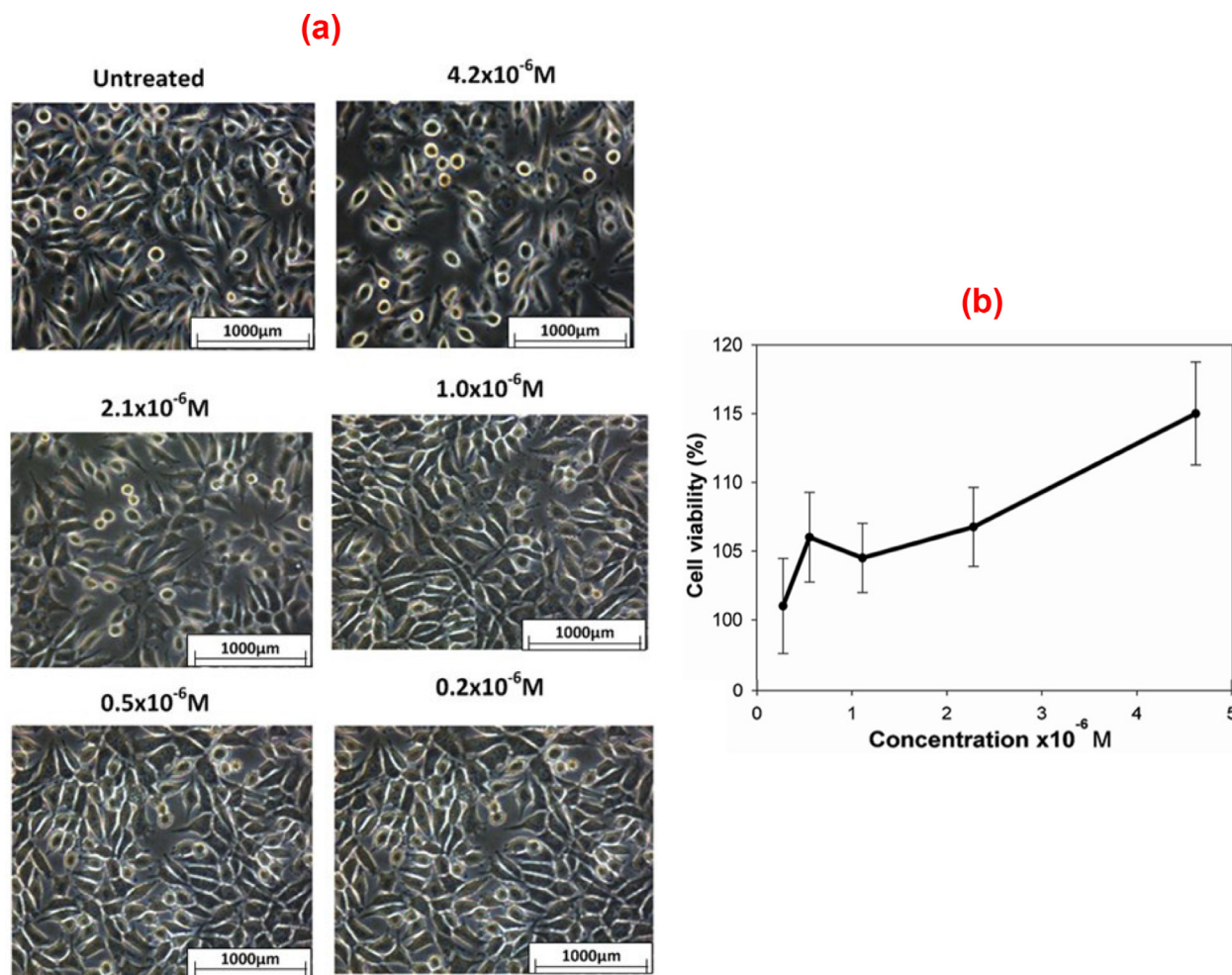


**Fig. 7** Dose-dependent cytotoxicity of the AuNPs conjugated BSA in SBF on L929 cell line: (a) morphology of L929 cells with and without AuNPs treatment and (b) effect of the concentration of the synthesized AuNPs on the viability of L929 cells.

siderable alteration in the morphology of L929 cells. It can be deduced that the synthesized AuNPs have a cytotoxic effect only on cancer cells. Some cancer cells contain protein, referred to as Epidermal Growth Factor Receptor (EGFR), over their surface, while the non-cancerous cells normally do not have a strong protein expression (Voldborg et al., 1997; Nicholson et al., 2001). The AuNPs interact with receptor molecules in the surface membrane of the cancer cell surface, resulting in delineation between cancer and normal cells.

### 3.6. Recognition of apoptosis

Apoptosis or also known as process in programmed cell death contributes in regulating the number of cells' developmental and physiological conditions by removing damaged cells. The increased in expression of mitochondrial apoptosis related proteins and loss of the mitochondrial membrane leading to stimulation of caspases responsible in controlling the death of cancer cells (Hu and Kavanagh, 2003; Ahmadian et al., 2017).

Apoptosis was investigated using flow cytometry to explore the effects of the synthesized AuNPs on HeLa cells. The SBF + BSA medium was used as the negative control (untreated sample). The samples were stained with FITC Annexin

V and PI to differentiate between viable cell populations, early apoptosis, and late apoptosis/necrosis. For untreated cells, 57 % and 3.62 % exhibited early and late apoptosis, respectively, signifying an overall apoptosis rate of 60.8 %. On the other hand, the treated cells exhibited early and late apoptosis rates of 78.8 % and 4.9 %, respectively, with an overall apoptosis rate of 82.7 % ( $p < 0.01$ ), as shown in Fig. 8. The toxicity of AuNPs is dependent on a range of physicochemical properties that include.

the chemical composition, crystal structure, shape, and size of the surface coating of AuNPs. The endocytic uptake of cells can affect the cytotoxicity of AuNPs. The Annexin V expression for AuNPs conjugated with BSA in SBF for 2 days on HeLa cells is shown in Fig. 8(a). FITC-A (horizontal) and PI-A (vertical) reveal Annexin V and PI stains intensity, respectively. The Q1, Q2, Q3, and Q4 parameters, denoting dead cells/debris, late apoptotic cells, live cells, and early apoptotic cells, respectively, and cell distribution (%) based on Annexin V/PI staining are presented in Fig. 8. The percentage of apoptotic cells was evaluated using flow cytometry. Data consists of representatives of three independent replicates, with the values indicating the mean of triplicate estimates. A significant difference was noted between the treated and untreated cells concerning overall apoptosis ( $p < 0.05$ ).

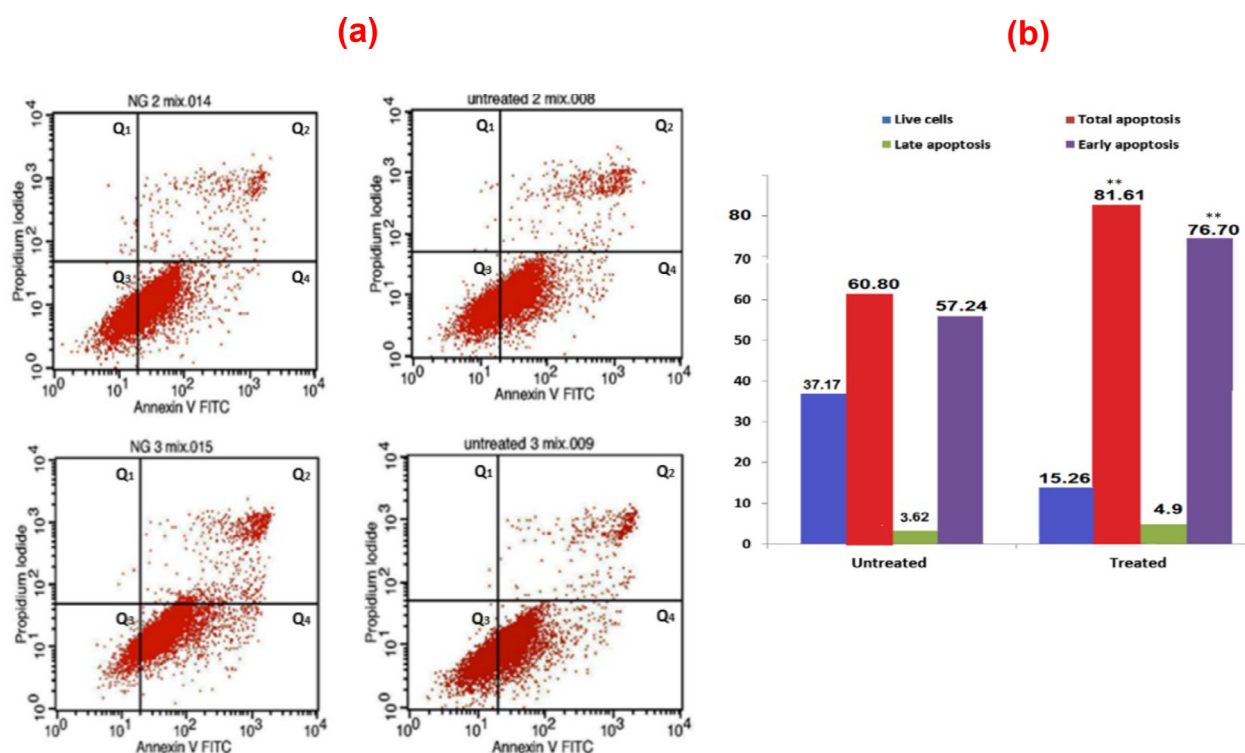


**Fig. 8** (a) Annexin V expression for AuNPs conjugated with BSA in SBF for 48 h on HeLa cells: FITC-A (horizontal) and PI-A (vertical) showed Annexin V and PI stains intensity respectively, Q1: dead cells/debris, Q2: late apoptotic cells, Q3: live cells, and Q4: early apoptotic cells and (b) cell distribution (%) based on Annexin V/PI staining.

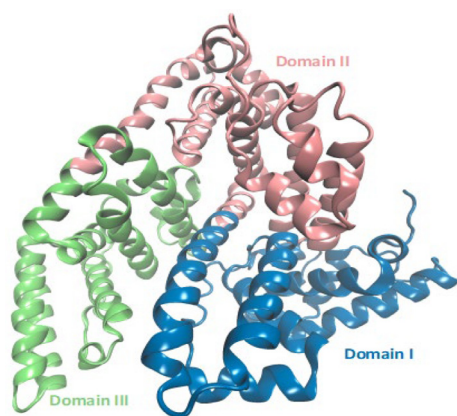


**Fig. 9** 3D model of Bovine serum albumin used in the construction of the simulated systems.

### 3.7. Computational details

The molecular dynamic simulation was utilized to investigate the nature of AuNPs conjugated with BSA (Au-BSA complexes) and the effect of salt concentration on the stability of those complexes. A model of a slab of Au was utilized to construct the Au-BSA simulated systems. BSA model (Fig. 9) was placed in ten diverse preliminary positions relative to the Au slab (Fig. 10) with the aim of exploring most of the conformational space of the bound complexes. Each of the ten systems was simulated at both high and low salt concentrations, result-

ing in a total of 20 Au-BSA systems with equal spacing between BSA and Au slab. In addition, two negative control simulations comprising only the BSA were performed at both high and low salt concentrations in the absence of the Au slab. The 22 systems were solvated with water, after which salt was added to each set of replicates to achieve the preferred concentration. All modelled systems were constructed in a way that mimics the experimental settings and all simulations were run for 100 ns. Overall, a spontaneous Au complexation took place early on during the simulation to reproduce the experimental outcomes for all 20 Au-BSA systems. After the initial interface, a stable Au-BSA complex was formed, where BSA sustained adsorption on Au surface without disassociation for the remainder of the 100 ns simulation in all 20 systems.

To explore the impact of salt concentration on the stability of the formed Au-BSA complexes, the stability of the higher-order structure of BSA was studied. Backbone RMSD of BSA relative to the initial structure was calculated for all systems, including the two -ve control simulations lacking the Au slab, for each set of salt concentration replicates, as shown in Fig. 11.

The average backbone RMSD values for the two AuNP-free simulations were 1.79 Å and 1.85 Å for low and high salt concentration simulations, respectively (Figure SI1). This suggests that salt concentration has a negligible effect on the stability of BSA in the absence of AuNPs. These findings correlates with a set of reported experimental studies, which explored the effect of salt concentration on the protein integrity (Mao et al., 2007, Sinha and Khare 2014). These studies demonstrates the dependence of protein integrity on the

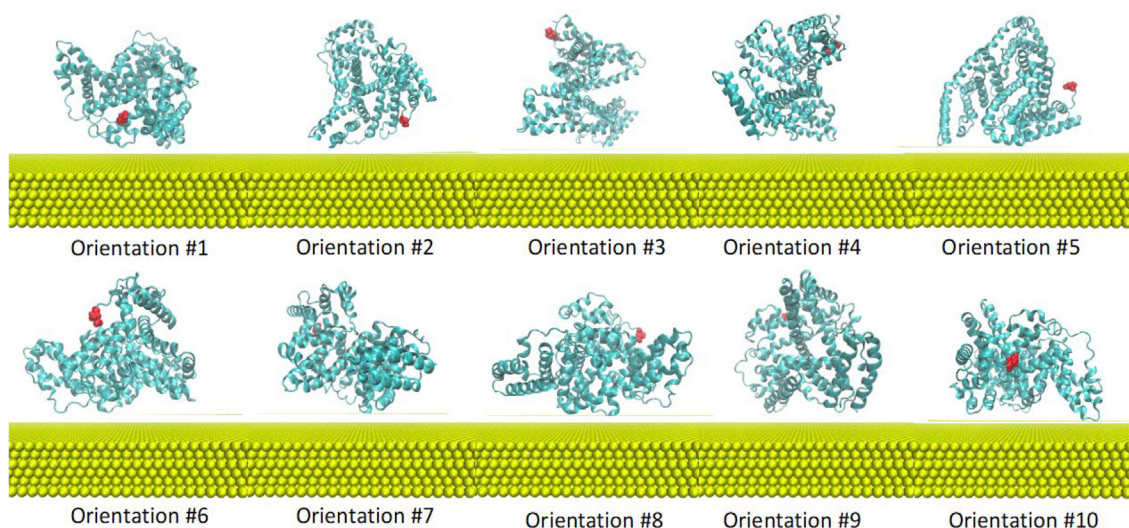


**Fig. 10** Ten initial orientations of BSA (cyan) in Au solution. Amino acid residue Asp1 in BSA is colored in red to highlight the different initial orientations of the replicates. Au slab is represented in yellow beads. Solvent and components are omitted for clarity.

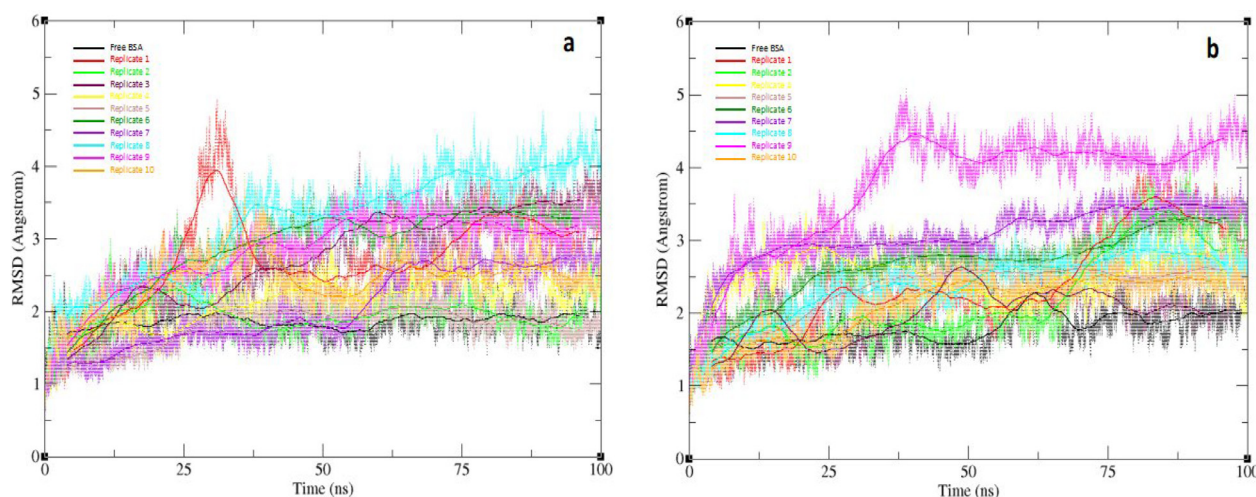


**Fig. 11** Backbone RMSD values with running average for simulation sets of high salt concentration (a) and low salt concentration (b) from 100 ns MD simulations for 10 initial orientations of BSA systems, and the free BSA as a negative control. Orientations 1, 2, 3, 4, 5, 6, 7, 8, 9, and 10 are represented in red, green, maroon, yellow, tan, emerald, violet, turquoise, magenta, and orange respectively with free BSA represented in black.

amount of ionizable residues within the protein that are water-exposed (Mao et al., 2007). In addition, higher salt concentrations can structurally stabilize halophilic proteins by initiating an acidic-residue-rich water exposed surface (Sinha and Khare 2014). Therefore, the observed non-effect of salt concentration on backbone RMSD for the free BSA simulations is possibly due to the nature of its water exposed surface, with a surface residue distribution that is possibly less susceptible to the effect of salt.

Conversely, for the Au-BSA complexes, almost all higher salt concentration replicates appear to display relatively lesser RMSDs throughout the simulations in contrast to their lower concentration counterparts. At a high salt concentration, the average backbone RMSD values for the 1st, 2nd, 3rd, 4th, 5th, 6th, 7th, 8th, 9th, and 10th orientations, were 2.69 Å,

1.94 Å, 2.13 Å, 2.03 Å, 1.75 Å, 2.66 Å, 2.04 Å, 3.01 Å, 2.72 Å and 2.30 Å, respectively. On the other hand, their corresponding average backbone RMSD values at a low salt concentration were 2.35 Å, 2.32 Å, 2.49 Å, 2.50 Å, 2.21 Å, 2.89 Å, 3.06 Å, 2.96 Å, 3.74 Å, and 2.27 Å, respectively. These results suggest that that increasing the salt concentration in a test solution serves an important role in the stabilization of the formed complexes. The atomic positional fluctuations were also calculated for each amino acid residue of BSA in all systems (Figure S12), which further supported the significant effect of Au-BSA complexes on the normal dynamics of BSA. Nonetheless, this effect was more apparent in the higher salt concentration set. The RMSD analysis indicated that Au-BSA complex produced from the 5th BSA orientation was the relatively most stable complex in both low and high salt con-

**Table 1** Au-BSA interface surface area calculated for the centroids of the top cluster from clustering MD simulations.

Au-BSA complex number	Au-BSA interface surface area (Low salt conc.) Å <sup>2</sup>	Au-BSA interface surface area (High salt conc.) Å <sup>2</sup>
Au-BSA Complex #1	1970	2077
Au-BSA Complex #2	1962	1829
Au-BSA Complex #3	2161	2256
Au-BSA Complex #4	2120	2461
Au-BSA Complex #5	3254	3193
Au-BSA Complex #6	2432	2707
Au-BSA Complex #7	1800	1828
Au-BSA Complex #8	2612	2402
Au-BSA Complex #9	1927	2129
Au-BSA Complex #10	3101	2844

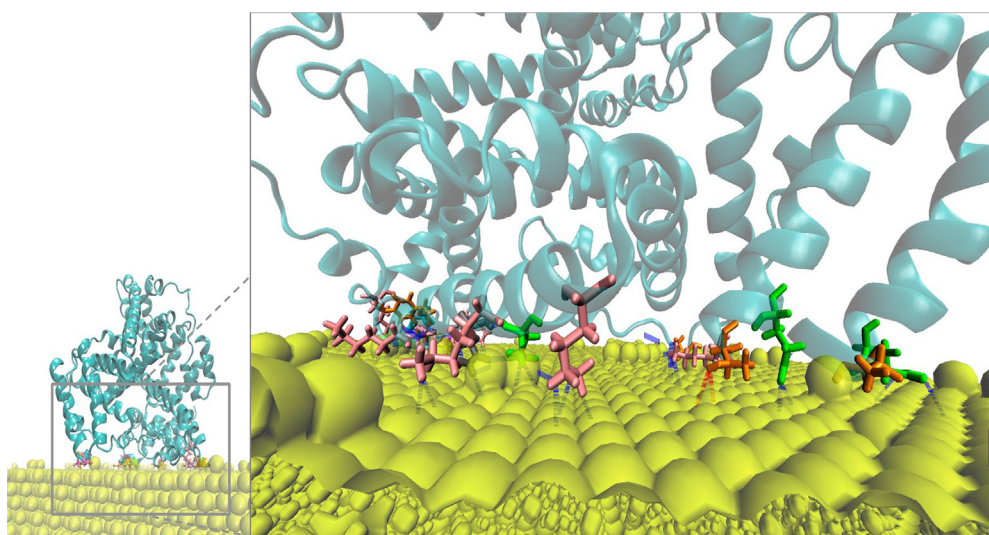


**Fig. 12** BSA residues involved in the interactions with the gold surface at the adsorption interface of replicate #5. Residues Lys, Thr, Gln, Cys, Asn, and His are represented in pink, orange, green, magenta, grey, and cyan sticks respectively. The rest of BSA is in transparent cyan ribbon and the gold particles in yellow spheres.

centrations, with the lowest backbone RMSD being 1.75 Å and 2.21 Å for the high and low concentration sets, respectively.

Clustering analysis was also performed on the last 50 ns from the 20 complex simulations to study the centroids of the top-ranked clusters of each simulation (Table SI1). The BSA surface area buried in the BSA-Au interaction interface was calculated for each simulation centroid (Table 1). The BSA interface surface area values indicate that BSA in the complex from the 5th orientation maintained a slightly larger contact surface area the gold slab, with an interaction interface surface area of 3254 Å<sup>2</sup> and 3193 Å<sup>2</sup> for the low and high concentration simulations, respectively. This correlates very well with the increased stability of this particular complex. In addition, calculating the number of stable salt bridges that formed within BSA throughout the MD simulations of the 5th complex in both salt concentration models confirms the stability of the structural integrity of BSA in these simulations. In total, 137 salt bridges were observed throughout the simulation of the 5th complex at the low salt concentration solution, whereas 145 interactions were observed throughout the higher salt con-

centration simulation. Again, this supports our hypothesis that the stability of the complex increases in a higher salt concentration solution.

To study protein-Au binding interactions between BSA and the surface of AuNPs at the interface of complex #5, ten snapshots evenly spaced during the last 50 ns of the 100 ns simulation were further analyzed. Among all BSA residues, the electrostatic interactions mediated by the amino acid residues lysine was largely the dominant, followed by threonine, cystine, glutamine, asparagine, and histidine, successively, as shown in Fig. 12. Earlier reports have analyzed the interactions between protein stabilizers and noble metal nanoparticles (Wang et al., 2016, Buglak and Kononov 2020). For instance, Wang A et al. investigated the impact of pH on the electrostatic interactions and reported that basic residues control the binding affinity of proteins to Au surface (Wang et al., 2016). A more current study proposed that the protonation state of amino acid residues on the exposed surface of a protein does not significantly influence their binding affinity to the surface of AuNPs (Buglak and Kononov 2020).

#### 4. Conclusion

This study successfully synthesized colloidal AuNPs of different sizes and narrow size distribution using pulsed laser ablation (Nd:YAG). In-situ and ex-situ AuNPs were conjugated with bovine serum albumin (BSA) in simulated body fluid (SBF). The synthesized AuNPs showed biocompatibility on L929 cells, but dose-dependent inhibition of cell viability on HeLa cells. Furthermore, wide-ranging molecular dynamic simulations infer that higher salt concentration in SBF solution advances the stability of the resulting AuNPs conjugated with BSA. The MD simulations showed that increased stability of Au-BSA complexes with higher salt concentration promotes the synthesis of nanoparticles with consistent size and shape, and is important for use in a variety of biomedical applications. Despite the increasing attention given to protein-stabilized noble metal NPs, little is understood regarding their interaction with the stabilizer protein at a molecular level. Computational methods are appropriate for elucidating these interactions in terms of types and preferred regions of protein for binding. Elucidating protein-Au binding will contribute to improving the effectiveness of experimental methods intended for developing protein-stabilized AuNPs. In general, the laser fragmentation process developed in this research can be valuable as a resource to generate AuNPs via a green synthesis procedure. The AuNPs could be suitable for cancer treatments. Additionally, this technique is an economical approach to the synthesis of AuNPs in a biological fluid that resembles blood plasma.

For future research, we would like to suggest an enhancement of the AuNPs study by including the experimental analysis on crystalline structural, elemental composition and binding energy of the colloidal AuNPs, particularly with different concentration of BSA and to expand the study on anticancer activities towards different type of cancerous cells for repeatability evaluation of AuNPs anticancer properties.

#### Declaration of Competing Interest

The authors declare that they have no known competing financial interests or personal relationships that could have appeared to influence the work reported in this paper.

#### Acknowledgements

The authors gratefully acknowledge the financial support of this research by the Ministry of Higher Education Malaysia for Fundamental Research Grant Scheme (Grant No. FRGS/1/2020/STG07/USM/02/8).

#### Appendix A. Supplementary material

Supplementary data to this article can be found online at <https://doi.org/10.1016/j.arabjc.2022.104395>.

#### References

- Abdulateef, S., Omar, A., Jafri, M.M., et al, 2017. One-step synthesis of stable colloidal gold nanoparticles through bioconjugation with bovine serum albumin in harsh environments. *J. Cluster Sci.* 28, 3193–3207.
- Adewale, O.B., Davids, H., Cairncross, L., et al, 2019. Toxicological behavior of gold nanoparticles on various models: influence of physicochemical properties and other factors. *Int. J. Toxicol.* 38, 357–384.
- Ahmadian, E., Eftekhari, A., Babaei, H., Nayebi, A. M., & Eghbal, M. A. (2017). Anti-cancer effects of citalopram on hepatocellular carcinoma cells occur via cytochrome C release and the activation of NF- $\kappa$ B. *Anti-Cancer Agents in Medicinal Chemistry (Formerly Current Medicinal Chemistry-Anti-Cancer Agents)*, 17(11), 1570–1577
- Alhussan, A., Bozdoğan, E.P.D., Chithrani, D.B., 2021. Combining gold nanoparticles with other radiosensitizing agents for unlocking the full potential of cancer radiotherapy. *Pharmaceutics* 13, 442.
- Ali, M.R., Wu, Y., El-Sayed, M.A., 2019. Gold-nanoparticle-assisted plasmonic photothermal therapy advances toward clinical application. *J. Phys. Chem. C* 123, 15375–15393.
- Al-Radadi, N.S., 2021. Facile one-step green synthesis of gold nanoparticles (AuNp) using licorice root extract: antimicrobial and anticancer study against HepG2 cell line. *Arabian J. Chem.* 14, 102956.
- Amendola, V., Meneghetti, M., 2013. What controls the composition and the structure of nanomaterials generated by laser ablation in liquid solution? *PCCP* 15, 3027–3046.
- Amendola, V., Pilot, R., Frascioni, M., et al, 2017. Surface plasmon resonance in gold nanoparticles: a review. *J. Phys.: Condens. Matter* 29, 203002.
- Arbyn, M., Weiderpass, E., Bruni, L., et al, 2020. Estimates of incidence and mortality of cervical cancer in 2018: a worldwide analysis. *Lancet Global Health* 8, e191–e203.
- Balasubramani, G., Ramkumar, R., Krishnaveni, N., et al, 2015. Structural characterization, antioxidant and anticancer properties of gold nanoparticles synthesized from leaf extract (decoction) of *Antigonon leptopus* Hook. & Arn. *J. Trace Elem. Med. Biol.* 30, 83–89.
- Baneshi, M., Dadfarnia, S., Shabani, A.M.H., et al, 2019. A novel theranostic system of AS1411 aptamer-functionalized albumin nanoparticles loaded on iron oxide and gold nanoparticles for doxorubicin delivery. *Int. J. Pharm.* 564, 145–152.
- Berman, H.M., Westbrook, J., Feng, Z., et al, 2000. The protein data bank. *Nucleic Acids Res.* 28, 235–242.
- Bhamidipati, M., Fabris, L., 2017. Multiparametric assessment of gold nanoparticle cytotoxicity in cancerous and healthy cells: the role of size, shape, and surface chemistry. *Bioconjug. Chem.* 28, 449–460.
- Bogdanov Jr, A.A., Gupta, S., Koshkina, N., et al, 2015. Gold nanoparticles stabilized with MPEG-grafted poly (l-lysine): in vitro and in vivo evaluation of a potential theranostic agent. *Bioconjug. Chem.* 26, 39–50.
- Botteon, C., Silva, L., Ccana-Capatinta, G., et al, 2021. Biosynthesis and characterization of gold nanoparticles using Brazilian red propolis and evaluation of its antimicrobial and anticancer activities. *Sci. Rep.* 11, 1–16.
- Bray, F., Ferlay, J., Soerjomataram, I., et al, 2018. Global cancer statistics 2018: GLOBOCAN estimates of incidence and mortality worldwide for 36 cancers in 185 countries. *CA Cancer J. Clin.* 68, 394–424.
- Bromma, K., Chithrani, D.B., 2020. Advances in gold nanoparticle-based combined cancer therapy. *Nanomaterials* 10, 1671.
- Buglak, A.A., Kononov, A.I., 2020. Comparative study of gold and silver interactions with amino acids and nucleobases. *RSC Adv.* 10, 34149–34160.
- Bujacz, A., 2012. Structures of bovine, equine and leporine serum albumin. *Acta Crystallogr. D Biol. Crystallogr.* 68, 1278–1289.
- Cai, W., Gao, T., Hong, H., et al, 2008. Applications of gold nanoparticles in cancer nanotechnology. *Nanotechnol., Sci. Appl.* 1, 17.
- Čempel, D., Nguyen, M.T., Ishida, Y., et al, 2018. l-Arginine-stabilized highly uniform Ag nanoparticles prepared in a microwave-induced plasma-in-liquid process (MWPLP). *Bull. Chem. Soc. Jpn.* 91, 362–367.

- Chansuvarn, W., Tuntulani, T., Imyim, A., 2015. Colorimetric detection of mercury (II) based on gold nanoparticles, fluorescent gold nanoclusters and other gold-based nanomaterials. *TrAC, Trends Anal. Chem.* 65, 83–96.
- Correard, F., Maximova, K., Estève, M.-A., et al, 2014. Gold nanoparticles prepared by laser ablation in aqueous biocompatible solutions: assessment of safety and biological identity for nanomedicine applications. *Int. J. Nanomed.* 9, 5415.
- Daduang, J., Palasap, A., Daduang, S., et al, 2015. Gallic acid enhancement of gold nanoparticle anticancer activity in cervical cancer cells. *Asian Pac. J. Cancer Prev.* 16, 169–174.
- Darden, T., York, D., Pedersen, L., 1993. Particle mesh Ewald: An  $N \log(N)$  method for Ewald sums in large systems. *J. Chem. Phys.* 98, 10089–10092.
- Dheyab, M.A., Aziz, A.A., Moradi Khaniabadi, P., et al, 2022. Monodisperse gold nanoparticles: a review on synthesis and their application in modern medicine. *Int. J. Mol. Sci.* 23, 7400.
- Dominguez-Medina, S., Blankenburg, J., Olson, J., et al, 2013. Adsorption of a protein monolayer via hydrophobic interactions prevents nanoparticle aggregation under harsh environmental conditions. *ACS Sustain. Chem. Eng.* 1, 833–842.
- Farooq, M.U., Novosad, V., Rozhkova, E.A., et al, 2018. Gold nanoparticles-enabled efficient dual delivery of anticancer therapeutics to HeLa cells. *Sci. Rep.* 8, 1–12.
- Freitas de Freitas, L., Varca, G.H.C., dos Santos Batista, J.G., et al, 2018. An overview of the synthesis of gold nanoparticles using radiation technologies. *Nanomaterials* 8, 939.
- Furusawa, H., Sakka, T., Ogata, Y.H., 2004. Characterization of ablated species in laser-induced plasma plume. *J. Appl. Phys.* 96, 975–982.
- Guerrini, L., Alvarez-Puebla, R.A., Pazos-Perez, N., 2018. Surface modifications of nanoparticles for stability in biological fluids. *Materials* 11, 1154.
- Harisha, K., Narayana, B., Sangappa, Y., 2021. Highly selective and sensitive colorimetric detection of arsenic (III) in aqueous solution using green synthesized unmodified gold nanoparticles. *J. Dispersion Sci. Technol.*, 1–12
- Harisha, K., Parushuram, N., Asha, S., et al, 2021. Eco-synthesis of gold nanoparticles by Sericin derived from Bombyx mori silk and catalytic study on degradation of methylene blue. *Part. Sci. Technol.* 39, 131–140.
- Hedei, P.H.M.A., Alsaee, S.K., Omar, A.F., et al, 2019. Spectral aging of gold and silver nanoparticles synthesized by laser ablation in liquids. *J. Nanophotonics* 13, 020502.
- Heinz, H., Lin, T.-J., Kishore Mishra, R., et al, 2013. Thermodynamically consistent force fields for the assembly of inorganic, organic, and biological nanostructures: the INTERFACE force field. *Langmuir* 29, 1754–1765.
- Hu, W., Kavanagh, J.J., 2003. Anticancer therapy targeting the apoptotic pathway. *Lancet Oncol.* 4 (12), 721–729.
- Humphrey, W., Dalke, A., Schulten, K., 1996. VMD: visual molecular dynamics. *J. Mol. Graph.* 14, 33–38.
- Huo, Q., Litherland, S.A., Sullivan, S., et al, 2012. Developing a nanoparticle test for prostate cancer scoring. *J. Transl. Med.* 10, 1–8.
- Hussain, S.M., Schlager, J.J., 2009. Safety evaluation of silver nanoparticles: inhalation model for chronic exposure. *Toxicol. Sci.* 108, 223–224.
- Irfan, M., Ahmad, T., Moniruzzaman, M., et al, 2020. Size and stability modulation of ionic liquid functionalized gold nanoparticles synthesized using *Elaeis guineensis* (oil palm) kernel extract. *Arabian J. Chem.* 13, 75–85.
- Jain, P.K., Lee, K.S., El-Sayed, I.H., et al, 2006. Calculated absorption and scattering properties of gold nanoparticles of different size, shape, and composition: applications in biological imaging and biomedicine. *J. Phys. Chem. B* 110, 7238–7248.
- Jeevanandam, J., Barhoum, A., Chan, Y.S., et al, 2018. Review on nanoparticles and nanostructured materials: history, sources, toxicity and regulations. *Beilstein J. Nanotechnol.* 9, 1050–1074.
- Kabashin, A.V., Delaporte, P., Pereira, A., et al, 2010. Nanofabrication with pulsed lasers. *Nanoscale Res. Lett.* 5, 454–463.
- Kalaivani, R., Maruthupandy, M., Muneeswaran, T., et al, 2020. Chitosan mediated gold nanoparticles against pathogenic bacteria, fungal strains and MCF-7 cancer cells. *Int. J. Biol. Macromol.* 146, 560–568.
- Kim, B., Song, W.C., Park, S.Y., et al, 2021. Green synthesis of silver and gold nanoparticles via *Sargassum serratifolium* extract for catalytic reduction of organic dyes. *Catalysts* 11, 347.
- Lassenberger, A., Grunewald, T., Van Oostrum, P., et al, 2017. Monodisperse Iron oxide nanoparticles by thermal decomposition: elucidating particle formation by second-resolved in situ small-angle X-ray scattering. *Chem. Mater.* 29, 4511–4522.
- Leve, F., Bonfim, D.P., Fontes, G., et al, 2019. Gold nanoparticles regulate tight junctions and improve cetuximab effect in colon cancer cells. *Nanomedicine* 14, 1565–1578.
- Li, S., Al-Misned, F.A., El-Serehy, H.A., et al, 2021. Green synthesis of gold nanoparticles using aqueous extract of *Mentha Longifolia* leaf and investigation of its anti-human breast carcinoma properties in the in vitro condition. *Arabian J. Chem.* 14, 102931.
- Li, L., Mu, Q., Zhang, B., et al, 2010. Analytical strategies for detecting nanoparticle–protein interactions. *Analyst* 135, 1519–1530.
- Liu, R., Pei, Q., Shou, T., et al, 2019. Apoptotic effect of green synthesized gold nanoparticles from *Curcuma wenyujin* extract against human renal cell carcinoma A498 cells. *Int. J. Nanomed.* 14, 4091.
- Mao, Y.-J., Sheng, X.-R., Pan, X.-M., 2007. The effects of NaCl concentration and pH on the stability of hyperthermophilic protein Ssh10b. *BMC Biochem.* 8, 1–8.
- Mitchell, M.J., Billingsley, M.M., Haley, R.M., et al, 2021. Engineering precision nanoparticles for drug delivery. *Nat. Rev. Drug Discovery* 20, 101–124.
- Nguyen, T.H.A., Nguyen, V.-C., Phan, T.N.H., et al, 2022. Novel biogenic silver and gold nanoparticles for multifunctional applications: Green synthesis, catalytic and antibacterial activity, and colorimetric detection of Fe (III) ions. *Chemosphere* 287, 132271.
- Nicholson, R.I., Gee, J.M.W., Harper, M.E., 2001. EGFR and cancer prognosis. *Eur. J. Cancer* 37, 9–15.
- Ordikhani, F., Erdem Arslan, M., Marcelo, R., et al, 2016. Drug delivery approaches for the treatment of cervical cancer. *Pharmaceutics* 8, 23.
- Oyane, A., Kim, H.M., Furuya, T., et al, 2003. Preparation and assessment of revised simulated body fluids. *J. Biomed. Mater. Res. Part A: Off. J. Soc. Biomater., Japanese Soc. Biomater., Australian Soc. Biomater. Korean Soc. Biomater.* 65, 188–195.
- Paidari, S., Ibrahim, S.A., 2021. Potential application of gold nanoparticles in food packaging: a mini review. *Gold Bull.* 54, 31–36.
- Patil, M.P., Jin, X., Simeon, N.C., et al, 2018. Anticancer activity of *Sasa borealis* leaf extract-mediated gold nanoparticles. *Artif. Cells Nanomed. Biotechnol.* 46, 82–88.
- Patil, M.P., Bayarara, E., Subedi, P., et al, 2019. Biogenic synthesis, characterization of gold nanoparticles using *Lonicera japonica* and their anticancer activity on HeLa cells. *J. Drug Delivery Sci. Technol.* 51, 83–90.
- Pelaz, B., Alexiou, C., Alvarez-Puebla, R.A., et al, 2017. Diverse applications of nanomedicine. *ACS Nano* 11, 2313–2381.
- Pérez-Juste, J., Pastoriza-Santos, I., Liz-Marzán, L.M., et al, 2005. Gold nanorods: synthesis, characterization and applications. *Coord. Chem. Rev.* 249, 1870–1901.
- Pierce, L. C., R. Salomon-Ferrer, C. Augusto F. de Oliveira, et al., 2012. Routine access to millisecond time scale events with accelerated molecular dynamics. *Journal of chemical theory and computation.* 8, 2997–3002.
- Qian, L., Su, W., Wang, Y., et al, 2019. Synthesis and characterization of gold nanoparticles from aqueous leaf extract of *Alternanthera*

- sessilis and its anticancer activity on cervical cancer cells (HeLa). *Artif. Cells Nanomed. Biotechnol.* 47, 1173–1180.
- Rajeshkumar, S., 2016. Anticancer activity of eco-friendly gold nanoparticles against lung and liver cancer cells. *J. Genet. Eng. Biotechnol.* 14, 195–202.
- Rehbock, C., Jakobi, J., Gamrad, L., et al, 2014. Current state of laser synthesis of metal and alloy nanoparticles as ligand-free reference materials for nano-toxicological assays. *Beilstein J. Nanotechnol.* 5, 1523–1541.
- Richter, K., Birkner, A., Mudring, A.-V., 2011. Stability and growth behavior of transition metal nanoparticles in ionic liquids prepared by thermal evaporation: how stable are they really? *PCCP* 13, 7136–7141.
- Roe, D.R., Cheatham III, T.E., 2013. PTRAJ and CPPTRAJ: software for processing and analysis of molecular dynamics trajectory data. *J. Chem. Theory Comput.* 9, 3084–3095.
- Roy, S., Liu, Z., Sun, X., et al, 2019. Assembly and degradation of inorganic nanoparticles in biological environments. *Bioconjug. Chem.* 30, 2751–2762.
- Sagvolden, G., 1999. Protein adhesion force dynamics and single adhesion events. *Biophys. J.* 77, 526–532.
- Salomon-Ferrer, R., Case, D.A., Walker, R.C., 2013. An overview of the Amber biomolecular simulation package. *Wiley Interdiscip. Rev.: Comput. Mol. Sci.* 3, 198–210.
- Scaiano, J.C., Stamplecoskie, K.G., Hallett-Tapley, G.L., 2012. Photochemical Norrish type I reaction as a tool for metal nanoparticle synthesis: importance of proton coupled electron transfer. *Chem. Commun.* 48, 4798–4808.
- Shao, J., Tanner, S.W., Thompson, N., et al, 2007. Clustering molecular dynamics trajectories: I. characterizing the performance of different clustering algorithms. *J. Chem. Theory Comput.* 3, 2312–2334.
- Shunmugam, R., Balusamy, S.R., Kumar, V., et al, 2021. Biosynthesis of gold nanoparticles using marine microbe (*Vibrio alginolyticus*) and its anticancer and antioxidant analysis. *J. King Saud Univ.-Sci.* 33, 101260.
- Singh, J., Dutta, T., Kim, K.-H., et al, 2018. ‘Green’ synthesis of metals and their oxide nanoparticles: applications for environmental remediation. *J. Nanobiotechnol.* 16, 1–24.
- Sinha, R., Khare, S.K., 2014. Protective role of salt in catalysis and maintaining structure of halophilic proteins against denaturation. *Front. Microbiol.* 5, 165.
- Sunderam, V., Thiagarajan, D., Lawrence, A.V., et al, 2019. In-vitro antimicrobial and anticancer properties of green synthesized gold nanoparticles using *Anacardium occidentale* leaves extract. *Saudi J. Biol. Sci.* 26, 455–459.
- Sylvestre, J.-P., Poulin, S., Kabashin, A.V., et al, 2004. Surface chemistry of gold nanoparticles produced by laser ablation in aqueous media. *J. Phys. Chem. B* 108, 16864–16869.
- Tabana, Y.M., Hassan, L.E.A., Ahamed, M.B.K., et al, 2016. Scopoletin, an active principle of tree tobacco (*Nicotiana glauca*) inhibits human tumor vascularization in xenograft models and modulates ERK1, VEGF-A, and FGF-2 in computer model. *Microvasc. Res.* 107, 17–33.
- Tan, M.I.S.M.H., Omar, A.F., Rashid, M., et al, 2019. VIS-NIR spectral and particles distribution of Au, Ag, Cu, Al and Ni nanoparticles synthesized in distilled water using laser ablation. *Results Phys.* 14, 102497.
- Tian, C., Kasavajhala, K., Belfon, K.A., et al, 2019. ff19SB: Amino-acid-specific protein backbone parameters trained against quantum mechanics energy surfaces in solution. *J. Chem. Theory Comput.* 16, 528–552.
- Torchilin, V., 2011. Tumor delivery of macromolecular drugs based on the EPR effect. *Adv. Drug Deliv. Rev.* 63, 131–135.
- Tsai, D.-H., DelRio, F.W., Keene, A.M., et al, 2011. Adsorption and conformation of serum albumin protein on gold nanoparticles investigated using dimensional measurements and in situ spectroscopic methods. *Langmuir* 27, 2464–2477.
- Upadhyayula, V.K., 2012. Functionalized gold nanoparticle supported sensory mechanisms applied in detection of chemical and biological threat agents: a review. *Anal. Chim. Acta* 715, 1–18.
- Vairavel, M., Devaraj, E., Shanmugam, R., 2020. An eco-friendly synthesis of *Enterococcus* sp.-mediated gold nanoparticle induces cytotoxicity in human colorectal cancer cells. *Environ. Sci. Pollut. Res.* 27, 8166–8175.
- Van der Zande, B.M., Böhmer, M.R., Fokkink, L.G., et al, 2000. Colloidal dispersions of gold rods: synthesis and optical properties. *Langmuir* 16, 451–458.
- Verma, M.S., Rogowski, J.L., Jones, L., et al, 2015. Colorimetric biosensing of pathogens using gold nanoparticles. *Biotechnol. Adv.* 33, 666–680.
- Voldborg, B.R., Damstrup, L., Spang-Thomsen, M., et al, 1997. Epidermal growth factor receptor (EGFR) and EGFR mutations, function and possible role in clinical trials. *Ann. Oncol.* 8, 1197–1206.
- Wahab, R., Dwivedi, S., Umar, A., et al, 2013. ZnO nanoparticles induce oxidative stress in Cloudman S91 melanoma cancer cells. *J. Biomed. Nanotechnol.* 9, 441–449.
- Wang, A., Perera, Y.R., Davidson, M.B., et al, 2016. Electrostatic interactions and protein competition reveal a dynamic surface in gold nanoparticle–protein adsorption. *J. Phys. Chem. C* 120, 24231–24239.
- Wang, L., Xu, J., Yan, Y., et al, 2019. Synthesis of gold nanoparticles from leaf *Panax notoginseng* and its anticancer activity in pancreatic cancer PANC-1 cell lines. *Artif. Cells Nanomed. Biotechnol.* 47, 1216–1223.
- Xu, X., Ho, W., Zhang, X., et al, 2015. Cancer nanomedicine: from targeted delivery to combination therapy. *Trends Mol. Med.* 21, 223–232.
- Yamada, K., Miyajima, K., Mafuné, F., 2007. Thermionic emission of electrons from gold nanoparticles by nanosecond pulse-laser excitation of interband. *J. Phys. Chem. C* 111, 11246–11251.
- Zhang, Y., Chen, F., Zhuang, J., et al, 2002. Synthesis of silver nanoparticles via electrochemical reduction on compact zeolite film modified electrodes. *Chem. Commun.*, 2814–2815.
- Zhang, X., Tan, Z., Jia, K., et al, 2019. *Rabdosia rubescens* Linn: green synthesis of gold nanoparticles and their anticancer effects against human lung cancer cells A549. *Artif. Cells Nanomed. Biotechnol.* 47, 2171–2178.